

# Chiral symmetry breaking in nearly conformal gauge theories \*

---

**Zoltán Fodor**

Department of Physics, University of Wuppertal  
Gaußstrasse 20, D-42119, Germany  
Email: [fodor@bodri.elte.hu](mailto:fodor@bodri.elte.hu)

**Kieran Holland**

Department of Physics, University of the Pacific  
3601 Pacific Ave, Stockton CA 95211, USA  
Email: [kholland@pacific.edu](mailto:kholland@pacific.edu)

**Julius Kuti**

Department of Physics 0319, University of California, San Diego  
9500 Gilman Drive, La Jolla, CA 92093, USA  
E-mail: [jkuti@ucsd.edu](mailto:jkuti@ucsd.edu)

**Dániel Nógrádi**

Department of Physics 0319, University of California, San Diego  
9500 Gilman Drive, La Jolla, CA 92093, USA  
Email: [nogradi@bodri.elte.hu](mailto:nogradi@bodri.elte.hu)

**Chris Schroeder**

Department of Physics 0319, University of California, San Diego  
9500 Gilman Drive, La Jolla, CA 92093, USA  
E-mail: [crs@physics.ucsd.edu](mailto:crs@physics.ucsd.edu)

We present new results on chiral symmetry breaking in nearly conformal gauge theories with fermions in the fundamental representation of the SU(3) color gauge group. The number of fermion flavors is varied in an extended range below the conformal window with chiral symmetry breaking ( $\chi$ SB) for all flavors between  $N_f = 4$  and  $N_f = 12$ . To identify  $\chi$ SB we apply several methods which include, within the framework of chiral perturbation theory, the analysis of the Goldstone spectrum in the p-regime and the spectrum of the fermion Dirac operator with eigenvalue distributions of random matrix theory in the  $\varepsilon$ -regime. Chiral condensate enhancement is observed with increasing  $N_f$  when the electroweak symmetry breaking scale  $F$  is held fixed in technicolor language. Important finite-volume consistency checks from the theoretical understanding of the  $SU(N_f)$  rotator spectrum of the  $\delta$ -regime are discussed. We also consider these gauge theories at  $N_f = 16$  inside the conformal window. The importance of understanding finite volume, zero momentum gauge field dynamics inside the conformal window is pointed out. Staggered lattice fermions with suppressed taste breaking are used throughout the simulations.

*The XXVII International Symposium on Lattice Field Theory - LAT2009*  
July 26-31 2009  
Peking University, Beijing, China

---

\*Based on talks at the conference by J. Kuti, D. Nogradi, and C.R. Schroeder.

## 1. Introduction

Our goal in this work to identify chiral symmetry breaking ( $\chi$ SB) below the conformal window of strongly interacting gauge theories requires the application and testing of several methods in finite volumes. These include the analysis of the Goldstone spectrum in the p-regime and the spectrum of the fermion Dirac operator with eigenvalue distributions of Random Matrix Theory (RMT) in the  $\varepsilon$ -regime, within the framework of chiral perturbation theory ( $\chi$ PT). Some critical consistency checks from the theoretical understanding of the  $SU(N_f)$  rotator spectrum of the  $\delta$ -regime will be also discussed. We report new results with  $N_f = 4, 8, 9, 12$  flavors with  $\chi$ SB below the conformal window for fermions in the fundamental representation of the  $SU(3)$  color gauge group. As  $N_f$  is increased, chiral condensate enhancement is observed when the electroweak symmetry breaking scale  $F$  is held fixed in technicolor language. We also discuss the theory inside the conformal window. The importance of understanding finite volume, zero momentum gauge field dynamics inside the conformal window is pointed out and illustrated at  $N_f = 16$ . Much of this work is an extension of our pre-conference publication [1] where we did not report our  $N_f = 12$  results. In a forthcoming publication [2] more details will be provided on the analysis and results presented here. Our work on the running coupling is presented separately [3].

It is an intriguing possibility that new physics beyond the Standard Model might take the form of some new strongly-interacting gauge theory building on the original technicolor idea [4, 5, 6]. This approach has lately been revived by new explorations of the multi-dimensional theory space of nearly conformal gauge theories [7, 8, 9, 10]. Model building of a strongly interacting electroweak sector requires the knowledge of the phase diagram of nearly conformal gauge theories as the number of colors  $N_c$ , number of fermion flavors  $N_f$ , and the fermion representation  $R$  of the technicolor group are varied in theory space. For fixed  $N_c$  and  $R$  the theory is in the chirally broken phase for low  $N_f$ , and asymptotic freedom is maintained with a negative  $\beta$  function. On the other hand, if  $N_f$  is large enough, the  $\beta$  function is positive for all couplings, and the theory is trivial. There is some range of  $N_f$  for which the  $\beta$  function might have a non-trivial zero, an infrared fixed point, where the theory is in fact conformal [13, 14]. This method has been refined by estimating the critical value of  $N_f$ , above which spontaneous chiral symmetry breaking no longer occurs [15, 16, 17].

Interesting models require the theory to be very close to, but below, the conformal window, with a running coupling which is almost constant over a large energy range [18, 19, 20, 21, 22, 23]. The nonperturbative knowledge of the critical  $N_f^{crit}$  separating the two phases is essential and this has generated much interest and many new lattice studies [1, 24, 25, 26, 27, 28, 29, 30, 31, 33, 32, 34, 35, 36, 37, 38, 39, 40, 41, 42, 43, 44, 45, 46, 47, 48, 49, 50, 51, 52, 53, 54, 55, 56]. To provide theoretical framework for the analysis of simulation results, we review first a series of tests expected to hold in the setting of  $\chi$ PT in finite volume and in the infinite volume limit.

## 2. Chiral symmetry breaking below the conformal window

We will identify in lattice simulations the chirally broken phases with  $N_f = 4, 8, 9, 12$  flavors of staggered fermions in the fundamental  $SU(3)$  color representation using finite volume analysis. We deploy staggered fermions with exponential (stout) smearing [57] in the lattice action to reduce

well-known cutoff effects with taste breaking in the Goldstone spectrum [58]. The presence of taste breaking requires a brief explanation of how we apply staggered  $\chi$ PT in our analysis. The important work of Lee, Sharpe, Aubin and Bernard [59, 60, 61] is closely followed in the discussion.

## 2.1 Staggered chiral perturbation theory

Starting with  $N_f = 4$  [59], the spontaneous breakdown of  $SU(4)_L \times SU(4)_R$  to vector  $SU(4)$  gives rise to 15 Goldstone and pseudo-Goldstone modes, described by fields  $\phi_i$  that can be organized into an  $SU(4)$  matrix

$$\Sigma(x) = \exp\left(i\frac{\phi}{\sqrt{2}F}\right), \quad \phi = \sum_{a=1}^{15} \phi_a T_a. \quad (2.1)$$

$F$  is the Goldstone decay constant in the chiral limit and the normalization  $T_a = \{\xi_\mu, i\xi_{\mu 5}, i\xi_{\mu\nu}, \xi_5\}$  is used for the flavor generators. The leading-order chiral Lagrangian is given by

$$\mathcal{L}_\chi^{(4)} = \frac{F^2}{4} \text{Tr}(\partial_\mu \Sigma \partial_\mu \Sigma^\dagger) - \frac{1}{2} B m_q F^2 \text{Tr}(\Sigma + \Sigma^\dagger), \quad (2.2)$$

with the fundamental parameters  $F$  and  $B$  measured on the technicolor scale  $\Lambda_{\text{TC}}$  which replaced  $\Lambda_{\text{QCD}}$  in the new theory. Expanding the chiral Lagrangian in powers of  $\phi$  one finds 15 degenerate Goldstone pions with masses given by

$$M_\pi^2 = 2Bm_q [1 + O(m_q/\Lambda_{\text{TC}})]. \quad (2.3)$$

The leading-order term is the tree-level result while the corrections come from loop diagrams and from higher-order terms in the chiral Lagrangian. The addition of  $a^2 \mathcal{L}_\chi^{(6)}$  breaks chiral symmetry and lifts the degeneracy of the Goldstone pions. Adding correction terms to Eq. (2.3) yields

$$M_\pi^2 = C(T_a) \cdot a^2 \Lambda_{\text{TC}}^4 + 2Bm_q [1 + O(m_q/\Lambda_{\text{TC}}) + O(a^2 \Lambda_{\text{TC}}^2)] \quad (2.4)$$

where the representation dependent  $C(T_a)$  is a constant of order unity. Contributions proportional to  $a^2$  are due to  $\mathcal{L}_\chi^{(6)}$  and lead to massive pseudo-Goldstone pions even in the  $m_q \rightarrow 0$  chiral limit, except for the Goldstone pion with flavor  $\xi_5$  which remains massless because the  $U(1)_A$  symmetry is protected.

Lee and Sharpe observe that the part of  $\mathcal{L}_\chi^{(6)}$  without derivatives, defining the potential  $\mathcal{V}_\chi^{(6)}$ , is invariant under flavor  $SO(4)$  transformations and gives rise to the  $a^2$  term in  $M_\pi^2$ . Terms in  $\mathcal{L}_\chi^{(6)}$  involving derivatives break  $SO(4)$  further down to the lattice symmetry group and give rise to non-leading terms proportional to  $a^2 m$  and  $a^4$ . The taste breaking potential is given by

$$\begin{aligned} -\mathcal{V}_\chi^{(6)} = & C_1 \text{Tr}(\xi_5 \Sigma \xi_5 \Sigma^\dagger) + C_2 \frac{1}{2} [\text{Tr}(\Sigma^2) - \text{Tr}(\xi_5 \Sigma \xi_5 \Sigma) + h.c.] \\ & + C_3 \frac{1}{2} \sum_{\nu} [\text{Tr}(\xi_\nu \Sigma \xi_\nu \Sigma) + h.c.] + C_4 \frac{1}{2} \sum_{\nu} [\text{Tr}(\xi_{\nu 5} \Sigma \xi_{\nu 5} \Sigma) + h.c.] \\ & + C_5 \frac{1}{2} \sum_{\nu} [\text{Tr}(\xi_\nu \Sigma \xi_\nu \Sigma^\dagger) - \text{Tr}(\xi_{\nu 5} \Sigma \xi_{\nu 5} \Sigma^\dagger)] + C_6 \sum_{\mu < \nu} \text{Tr}(\xi_{\mu\nu} \Sigma \xi_{\mu\nu} \Sigma^\dagger). \end{aligned} \quad (2.5)$$

The six unknown coefficients  $C_i$  are all of size  $\Lambda_{\text{TC}}^6$ .

In the continuum, the Goldstone pions form a 15-plet of flavor  $SU(4)$  and are degenerate. On the lattice, states are classified by the symmetries of the transfer matrix, and the pseudo-Goldstone pions fall into 7 irreducible representations: four 3-dimensional representations with flavors  $\xi_i$ ,  $\xi_{i5}$ ,  $\xi_{ij}$  and  $\xi_{i4}$ , and three 1-dimensional representations with flavors  $\xi_4$ ,  $\xi_{45}$  and  $\xi_5$ .

Close to both the chiral and continuum limits, the pseudo-Goldstone masses are given by

$$M_\pi(T_a)^2 = 2Bm_q + a^2\Delta(T_a) + O(a^2m_q) + O(a^4), \quad (2.6)$$

with  $\Delta(T_a) \sim \Lambda_{\text{TC}}^4$  arising from  $\mathcal{V}_\chi^{(6)}$ . Since  $\mathcal{V}_\chi^{(6)}$  respects flavor  $SO(4)$ , the 15 Goldstone particles fall into  $SO(4)$  representations:

$$\begin{aligned} \Delta(\xi_5) &= 0, \quad \Delta(\xi_\mu) = \frac{8}{F^2}(C_1 + C_2 + C_3 + 3C_4 + C_5 + 3C_6), \\ \Delta(\xi_{\mu 5}) &= \frac{8}{F^2}(C_1 + C_2 + 3C_3 + C_4 - C_5 + 3C_6), \quad \Delta(\xi_{\mu\nu}) = \frac{8}{F^2}(2C_3 + 2C_4 + 4C_6). \end{aligned} \quad (2.7)$$

In the chiral limit at finite lattice spacing, the lattice irreducible representations with flavors  $\xi_i$  and  $\xi_4$  are degenerate, those with flavors  $\xi_{i5}$  and  $\xi_{45}$ , and those with flavors  $\xi_{ij}$  and  $\xi_{i4}$  are degenerate as well. No predictions can be made for the ordering, splittings, or even the *signs* of the mass shifts. Our simulations indicate that they are all positive with the exponentially smeared staggered action we use, making the existence of an Aoki phase [59] unlikely. The method of [59] has been generalized to the  $N_f > 4$  case [60, 61] which we adopted in our calculations with help from Bernard and Sharpe. The procedure cannot be reviewed here but it will be used in the interpretation of our  $N_f = 8$  simulations.

## 2.2 Finite volume analysis in the p-regime

Three different regimes can be selected in simulations to identify the chirally broken phase from finite volume spectra and correlators. For a lattice size  $L_s^3 \times L_t$  in euclidean space and in the limit  $L_t \gg L_s$ , the conditions  $F_\pi L_s > 1$  and  $M_\pi L_s > 1$  select the p-regime, in analogy with low momentum counting [62, 63].

For arbitrary  $N_f$ , in the continuum and in infinite volume, the one-loop chiral corrections to  $M_\pi$  and  $F_\pi$  of the degenerate Goldstone pions are given by

$$M_\pi^2 = M^2 \left[ 1 - \frac{M^2}{8\pi^2 N_f F^2} \ln \left( \frac{\Lambda_3}{M} \right) \right], \quad (2.8)$$

$$F_\pi = F \left[ 1 + \frac{N_f M^2}{16\pi^2 F^2} \ln \left( \frac{\Lambda_4}{M} \right) \right], \quad (2.9)$$

where  $M^2 = 2B \cdot m_q$  and  $F, B, \Lambda_3, \Lambda_4$  are four fundamental parameters of the chiral Lagrangian, and the small quark mass  $m_q$  explicitly breaks the symmetry [64]. The chiral parameters  $F, B$  appear in the leading part of the Lagrangian in Eq. (2.2), while  $\Lambda_3, \Lambda_4$  enter in next order. There is the well-known GMOR relation  $\Sigma_{\text{cond}} = BF^2$  in the  $m_q \rightarrow 0$  limit for the chiral condensate per unit flavor [65]. It is important to note that the one-loop correction to the pion coupling constant  $F_\pi$  is enhanced by a factor  $N_f^2$  compared to  $M_\pi^2$ . The chiral expansion for large  $N_f$  will break down for  $F_\pi$  much faster for a given  $M_\pi/F_\pi$  ratio. The NNLO terms have been recently calculated [66] showing potentially dangerous  $N_f^2$  corrections to Eqs. (2.8, 2.9).

The finite volume corrections to  $M_\pi$  and  $F_\pi$  are given in the p-regime by

$$M_\pi(L_s, \eta) = M_\pi \left[ 1 + \frac{1}{2N_f} \frac{M^2}{16\pi^2 F^2} \cdot \tilde{g}_1(\lambda, \eta) \right], \quad (2.10)$$

$$F_\pi(L_s, \eta) = F_\pi \left[ 1 - \frac{N_f}{2} \frac{M^2}{16\pi^2 F^2} \cdot \tilde{g}_1(\lambda, \eta) \right], \quad (2.11)$$

where  $\tilde{g}_1(\lambda, \eta)$  describes the finite volume corrections with  $\lambda = M \cdot L_s$  and aspect ratio  $\eta = L_t/L_s$ . The form of  $\tilde{g}_1(\lambda, \eta)$  is a complicated infinite sum which contains Bessel functions and requires numerical evaluation [63]. Eqs. (2.8-2.11) provide the foundation of the p-regime fits in our simulations.

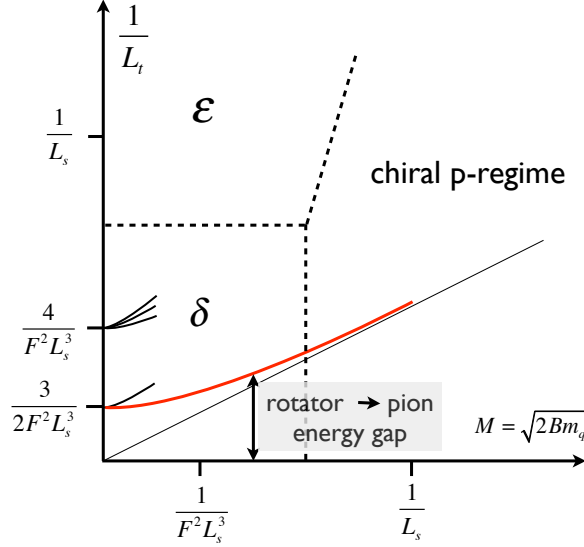


**Figure 1:** Schematic plot of the regions in which the three low energy chiral expansions are valid. The vertical axis shows the finite temperature scale (euclidean time in the path integral) which probes the rotator dynamics of the  $\delta$ -regime and the  $\varepsilon$ -regime. The first two low lying rotator levels are also shown on the vertical axis for the simple case of  $N_f = 2$ . The fourfold degenerate lowest rotator excitation at  $m_q = 0$  will split into an isotriplet state (lowest energy level), which evolves into the p-regime pion as  $m_q$  increases, and into an isosinglet state representing a multi-pion state in the p-regime. Higher rotator excitations have similar interpretations.

### 2.3 $\delta$ -regime and $\varepsilon$ -regime

At fixed  $L_s$  and in cylindrical geometry  $L_t/L_s \gg 1$ , a crossover occurs from the p-regime to the  $\delta$ -regime when  $m_q \rightarrow 0$ , as shown in Fig. 1. The dynamics is dominated by the rotator states of the chiral condensate in this limit [67] which is characterized by the conditions  $FL_s > 1$  and  $ML_s \ll 1$ . The densely spaced rotator spectrum scales with gaps of the order  $\sim 1/F^2 L_s^3$ , and at  $m_q = 0$  the chiral symmetry is apparently restored. However, the rotator spectrum, even at  $m_q = 0$  in the finite volume, will signal that the infinite system is in the chirally broken phase for the particular parameter set of the Lagrangian. This is often misunderstood in the interpretation of lattice simulations. Measuring finite energy levels with pion quantum numbers at fixed  $L_s$  in the  $m_q \rightarrow 0$  limit is not a signal for chiral symmetry restoration of the infinite system [41].

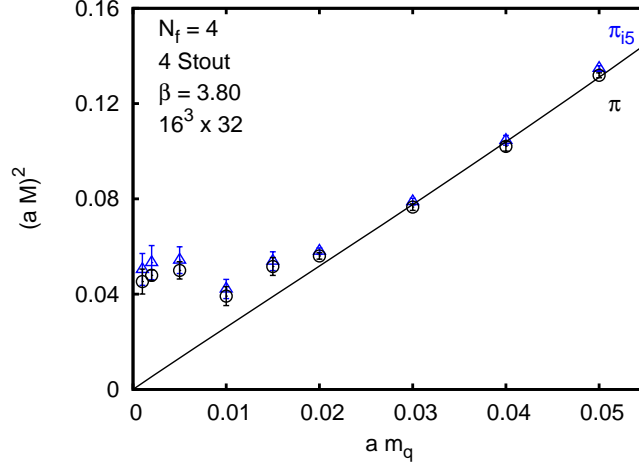


**Figure 2:** The crossover from the p-regime to the  $\delta$ -regime is shown for the  $\pi$  and  $\pi_{15}$  states at  $N_f = 4$ .

If  $L_t \sim L_s$  under the conditions  $FL_s > 1$  and  $ML_s \ll 1$ , the system will be driven into the  $\varepsilon$ -regime which can be viewed as the high temperature limit of the  $\delta$ -regime quantum rotator. Although the  $\delta$ -regime and  $\varepsilon$ -regime have an overlapping region, there is an important difference in their dynamics. In the  $\delta$ -regime of the quantum rotator, the mode of the pion field  $U(x)$  with zero spatial momentum dominates with time-dependent quantum dynamics. The  $\varepsilon$ -regime is dominated by the four-dimensional zero momentum mode of the chiral Lagrangian.

We report simulation results of all three regimes in the chirally broken phase of the technicolor models we investigate. The analysis of the three regimes complement each other and provide cross-checks for the correct identification of the phases. First, we will probe Eqs. (2.8-2.11) in the p-regime, and follow with the study of Dirac spectra and RMT eigenvalue distributions in the  $\varepsilon$ -regime. The spectrum in the  $\delta$ -regime is used as a signal to monitor p-regime spectra as  $m_q$  decreases. Fig. 2 is an illustrative example of this crossover in our simulations. It is important to note that the energy levels in the chiral limit do not match the rotator spectrum at the small  $F \cdot L_s$  values of the simulations. This squeezing with  $F \cdot L_s$  not large enough for undistorted, finite volume, chiral behavior in the p-regime,  $\varepsilon$ -regime, and  $\delta$ -regime, will be further discussed in our p-regime simulations presented next. We will also describe some methods to put this squeezing into a more quantitative context.

### 3. Goldstone spectra and $\chi$ SB from simulations at $N_f = 4$ in the p-regime

In this section we describe in some detail the methods we use for successfully testing chiral symmetry breaking. Our tests in the p-regime have two major components. The primary test is to identify the pseudo-Goldstone spectrum of the staggered formulation with evidence for recovery from taste symmetry breaking close to the continuum limit. The secondary test is to probe chiral loop corrections to the tree-level behavior of  $M_\pi^2$  and  $F_\pi$  as the fermion mass  $a \cdot m_q$  is varied at fixed gauge coupling  $\beta$ . The evidence we find for chiral symmetry breaking at  $N_f = 4, 8, 9, 12$  is common to all flavors. Limitations and ambiguities identified at  $N_f = 4$  for future improvements are expected to be more pronounced with increasing  $N_f$ . Results for each flavor we have simulated in

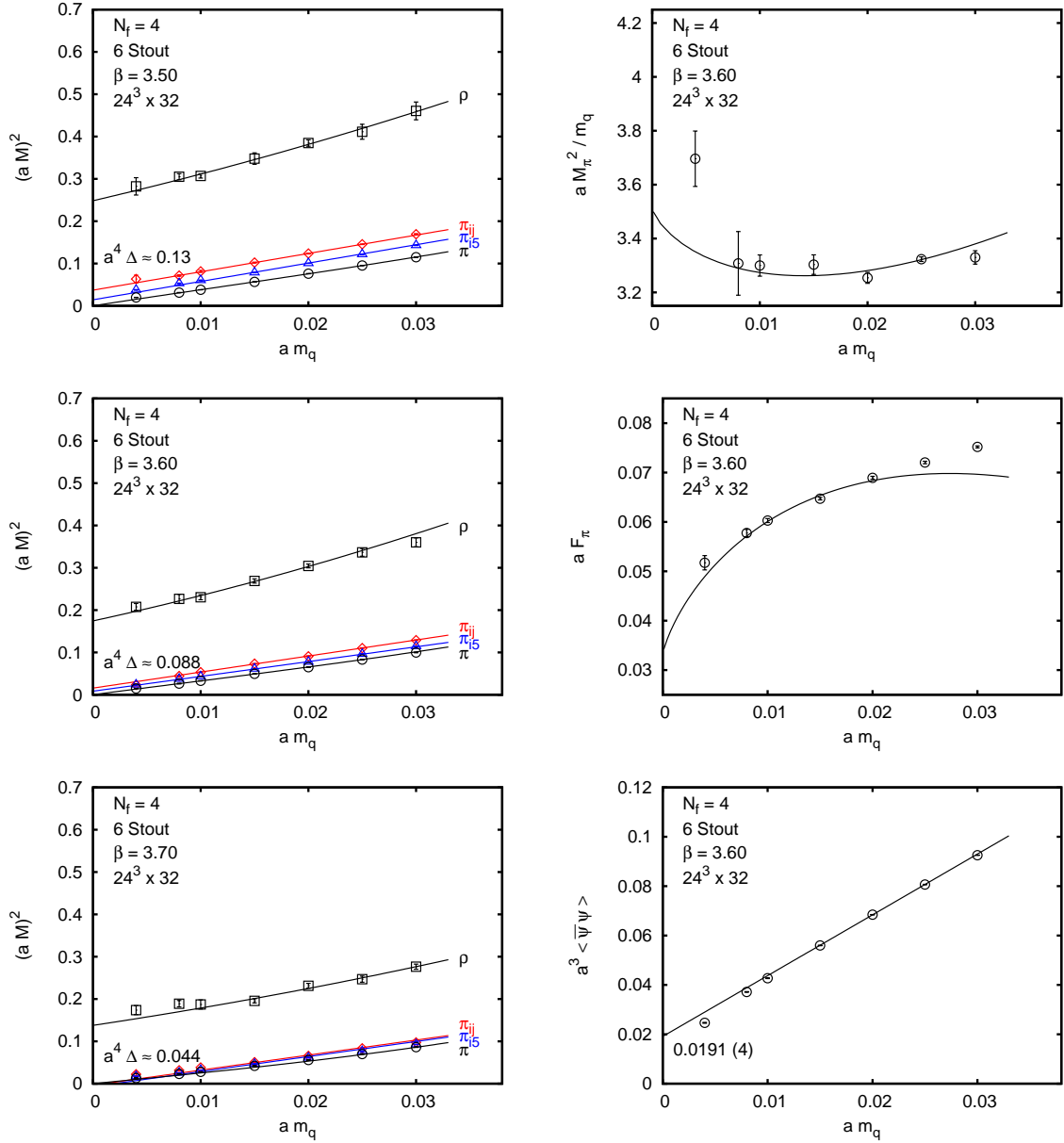


**Figure 3:** The Goldstone spectrum and chiral fits are shown for simulations with lattice size  $24^3 \times 32$ . The left column shows the pseudo-Goldstone spectrum with decreasing taste breaking as the gauge coupling is varied from  $\beta = 3.5$  to  $\beta = 3.7$ . The middle value at  $\beta = 3.6$  was chosen for chiral fits which are shown in the right column. The top right figure with fitting range  $a \cdot m_q = 0.008 - 0.025$  shows the NLO chiral fit to  $M_\pi^2/m_q$  which approaches  $2B$  in the chiral limit. Data points below  $m_q = 0.008$  are not in the chiral p-regime and not used in the fitting procedure. The middle figure on the right is the NLO chiral fit to  $F_\pi$  in the range  $a \cdot m_q = 0.008 - 0.02$ . The bottom right figure is the linear fit to the chiral condensate with fitting range  $a \cdot m_q = 0.015 - 0.025$ . The physical fit parameters  $B, F, \Lambda_3, \Lambda_4$  are discussed in the text.

the p-regime are presented in separate sections beginning here with general discussion and  $N_f = 4$  results.

We have used the tree-level Symanzik-improved gauge action for all simulations. The con-

ventional  $\beta = 6/g^2$  lattice gauge coupling is defined as the overall factor in front of the three well-known terms of the lattice action. The link variables in the staggered fermion matrix were exponentially smeared with six stout steps at  $N_f = 4$  and the RHMC algorithm was deployed in all runs. The results shown in Fig. 3 are from the p-regime of  $\chi$ SB with the conditions  $M_\pi \cdot L_s \gg 1$  and  $F_\pi \cdot L_s \sim 1$  when the chiral condensate begins to follow the expected behavior of infinite-volume chiral perturbation theory from Eqs. (2.8,2.9) in next-to-leading order (NLO) with calculable finite volume corrections from Eqs. (2.10,2.11) which are negligible at  $L_s = 24$ . We have empirical evidence that the  $M_\pi$  and  $F_\pi$  data points are free of finite volume corrections in practically the entire fitting range of the fermion masses we use at  $L_s = 24$  so that the negligible corrections from Eqs. (2.10,2.11) can be ignored.

Within some finite volume limitations, which we will address, the  $N_f = 4$  simulations work in the p-regime as expected. The left column of Fig. 3 shows that the pseudo-Goldstone spectrum clearly remains separated from the hadronic scale of the  $\rho$ -meson as  $\beta$  is varied. Moving towards the continuum limit with increasing  $\beta$ , we see the split pseudo-Goldstone spectrum collapsing into the degenerate continuum pion spectrum. The true Goldstone pion whose mass will vanish in the  $a \cdot m_q = 0$  limit at fixed lattice spacing and two additional split states with small residual masses at  $a \cdot m_q = 0$  are shown to illustrate the trend.  $a^4 \Delta$  is the measure of the small taste breaking in quadratic mass splitting as measured in lattice units. The origin of the splittings and the quantum numbers were discussed in Section 2 as shown in Eq. (2.7). The spectrum is approximately parallel as the bare fermion mass  $a \cdot m_q$  is varied at fixed lattice spacing and the gaps appear to be equally spaced to a good approximation, consistent with earlier observations in QCD where the  $C_4$  term seems to dominate staggered taste breaking for two light flavors with equally spaced pseudo-Goldstone levels [59]. We selected  $\beta = 3.6$  for testing  $\chi$ PT of finite volume Goldstone dynamics in the p-regime. This choice with small taste breaking is close to the continuum limit without excessive squeeze on the important product  $F \cdot L_s$  which in an ideal simulation of the p-regime should be large ( $F$  is the chiral limit of  $F_\pi$  as  $a \cdot m_q \rightarrow 0$  at fixed lattice spacing).

The simultaneous chiral fit of  $M_\pi^2/m_q$  and  $F_\pi$  based on Eqs. (2.8-2.11) is shown in Fig. 3 where chiral loops correct the tree-level values of  $M_\pi^2/m_q = 2B$  and  $F_\pi$ . In the fitting range  $a \cdot m_q = 0.008 - 0.025$  applied to  $M_\pi^2/m_q$  we observe small corrections to the tree-level value of  $2B$  which keeps the fit well within the range of one-loop  $\chi$ PT. In the fitting range  $a \cdot m_q = 0.008 - 0.02$  the  $F_\pi$  data are about a factor of two larger than  $F$  which indicates how the one-loop fit is being pushed to its limits. Without loop correction  $F_\pi$  would not change from its fitted value of  $a \cdot F = 0.033(4)$  in the chiral limit at fixed lattice spacing. The fitted value of  $B$  is  $a \cdot B = 1.76(7)$  in lattice units and  $M_\rho/F = 13(1)$  in the chiral limit (the linear fit of  $M_\rho = c + d \cdot m_q$  is used at all  $N_f$  values to determine  $M_\rho(m_q = 0)$ ). The fitted value of  $B/F = 53(6)$  indicates significant enhancement of the chiral condensate from its  $N_f = 2$  value [53, 68]. In our simultaneous fits we get  $\Lambda_3 = 0.37(5)$  and  $\Lambda_4 = 0.51(1)$  which set the chiral couplings in the NLO chiral Lagrangian.

The chiral condensate  $\langle \bar{\psi}\psi \rangle$  summed over all flavors is dominated by the linear term in  $m_q$  from UV contributions. The linear fit gives  $\langle \bar{\psi}\psi \rangle = 0.0191(4)$  in the chiral limit which differs from the GMOR relation of  $\langle \bar{\psi}\psi \rangle = 4F^2B$  by about a factor of two with  $4F^2B = 0.008(2)$  fitted. There are several sources of this disagreement. The chiral log in  $\langle \bar{\psi}\psi \rangle$  will bring further down the true fitted value in the chiral limit. Our volumes are not large enough yet to attempt a sensible chiral log fit to the condensate at small  $a \cdot m_q$  values. Finite volume squeezing effects distort the consistency of

the results in our limited range of simulation volumes. The choice of fitting method to Eqs. (2.8,2.9) can also have some effect on the results. On the right-hand sides of the equations, the variable pair  $(M, F)$  in the chiral logs can be replaced with the pair  $(M_\pi, F_\pi)$  which is equivalent to a partial resummation [68]. This will be reported in our more detailed forthcoming journal publication [2].

Finite volume limitations when measured in  $F$  units have the biggest effect on our chiral analysis. The value  $F \cdot L_s \approx 0.8$  is not expected to protect against significant finite-volume squeezing effects for even the largest spatial size  $L_s = 24$  used in the chiral fits at  $N_f = 4$ . Larger than optimal NLO corrections in the chiral fits of  $F_\pi$  and finite-volume squeezing effects are closely related concerns. Simulations on larger lattices would increase  $F \cdot L_s$  and allow us to drop back in  $a \cdot m_q$  into a more comfortable range with smaller NLO chiral corrections for  $F_\pi$ .

Finite volume corrections to the rotator spectrum in the  $\delta$ -regime set some quantitative measure of squeezing effects on the chiral analysis. The connection is made by observing that the pion spectrum in the p-regime can be viewed at fixed spatial volume  $L_s^3$  as the adiabatic evolution from the energy levels of the rotator spectrum of the  $\delta$ -regime as illustrated schematically in Fig. 2 for the lowest  $N_f = 2$  rotator levels. The rotator spectrum for  $N_f = 2$  is given by  $E_l = \frac{1}{2\Theta}l(l+2)$ , with  $l = 0, 1, 2, \dots$ , where the moment of inertia is calculated in NLO [69, 70] as  $\Theta = F^2 L_s^3 (1 + \frac{C(N_f=2)}{F^2 L_s^2} + O(\frac{1}{F^4 L_s^4}))$ . The value of  $C(N_f = 2)$  is known to be 0.45 and is expected to grow with  $N_f$ . At  $F \cdot L_s \approx 0.8$  the correction is 70% for  $N_f = 2$  and probably considerably larger for  $N_f = 4$ . The leading-order rotator gap for arbitrary  $N_f$  is given by  $E_1 - E_0 = \frac{N_f - 1}{N_f F^2 L_s^3}$  but the coefficient  $C(N_f)$  is an important missing piece in the analysis. Were we to continue the p-regime Goldstone spectrum at  $N_f = 4$ ,  $L_s = 24$ , and  $\beta = 3.6$  to the  $\delta$ -regime adiabatically, the small value of  $F \cdot L_s$  would not allow us to get a reliable estimate of  $F$  based on the chiral rotator spectrum with the collapse of the adiabatic approximation. This is a quantitative warning sign of the need for considerably larger spatial volume for robust p-regime results to determine  $F$  in the chiral fitting procedure. In fact, we are going to fit  $M_\pi^2/m_q$  in the chiral analysis for  $N_f = 8, 9, 12$  with better controlled NLO loop corrections, but  $F_\pi$  will not be fitted. For larger  $N_f$ , a reliable simultaneous fit requires substantially larger volumes than are realistic with our current resources.

In summary, the  $N_f = 4$  system passed both tests in the chirally broken phase and shows significant enhancement of the chiral condensate when measured in units of the electroweak symmetry breaking scale set by  $F$ . This is a relevant effect to monitor for fermion mass generation in extended technicolor applications as we begin to approach the conformal window [53].

#### 4. Goldstone spectrum and $\chi$ SB from simulations at $N_f = 8$ in the p-regime

As we move to the  $N_f = 8$  p-regime simulations, we can clearly identify the p-regime of the chirally broken phase as summarized in Fig. 4. The same lattice action and algorithm was used for the  $N_f = 8$  p-regime simulations as introduced earlier for  $N_f = 4$ . We can clearly identify the pseudo-Goldstone spectrum which is separated from the technicolor scale of the  $\rho$ -meson. Moving towards the continuum limit we observe at  $\beta = 1.4$  the split pion spectrum collapsing toward the true Goldstone pion with a new distinct feature. The true Goldstone pion, whose mass will vanish in the  $a \cdot m_q = 0$  limit at fixed lattice spacing, and two additional split pseudo-Goldstone states appear with considerably different slopes in Fig. 4 as  $m_q$  increases. For small  $a \cdot m_q$  we find the

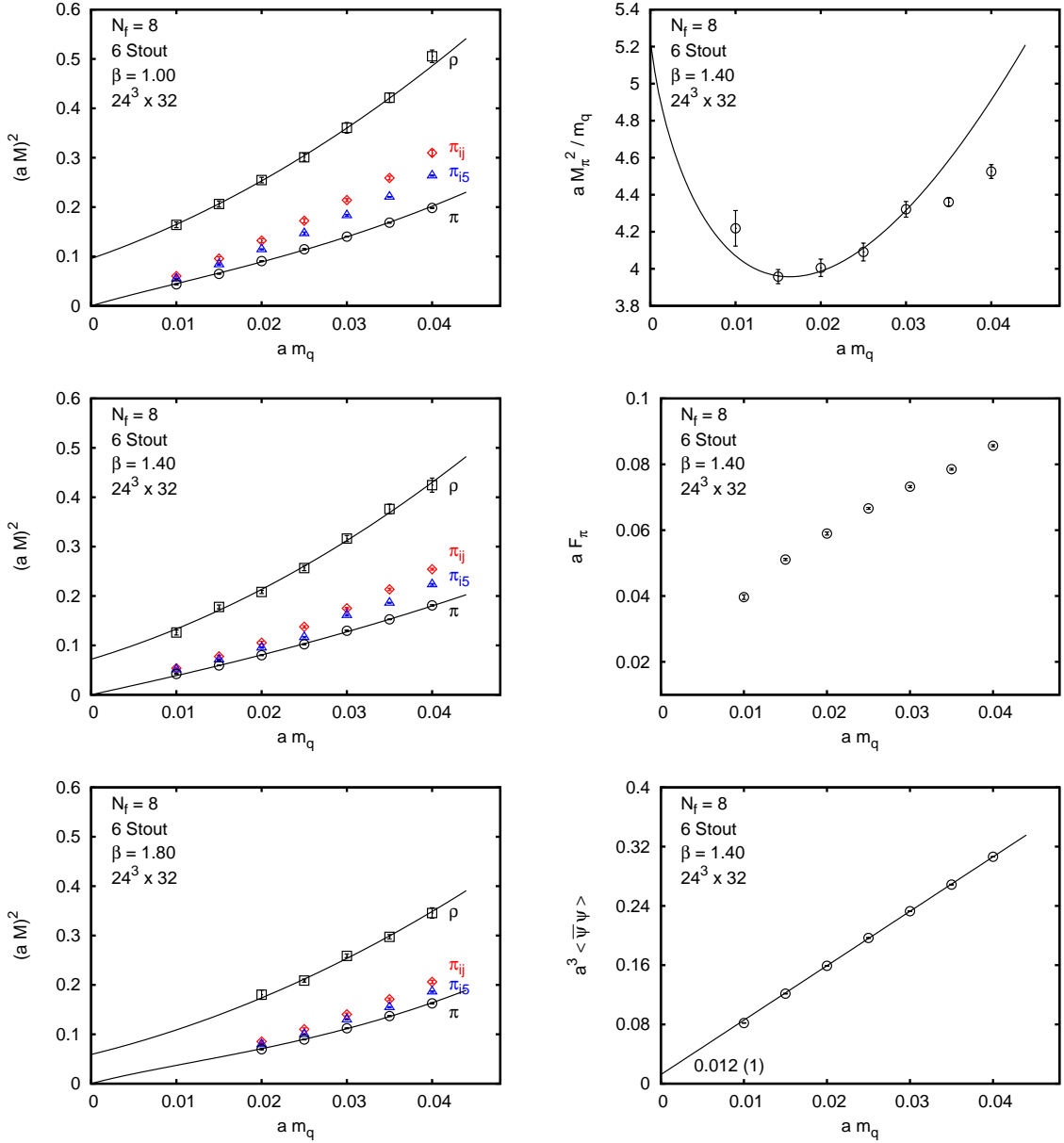


**Figure 4:** The Goldstone spectrum and chiral fits are shown for  $N_f = 8$  simulations with lattice size  $24^3 \times 32$ . The left column shows the pseudo-Goldstone spectrum with decreasing taste breaking as the gauge coupling is varied from  $\beta = 1.0$  to  $\beta = 1.8$ . The middle value at  $\beta = 1.4$  was chosen in the top right figure with fitting range  $a \cdot m_q = 0.015 - 0.03$  of the NLO chiral fit to  $M_\pi^2/m_q$  which approaches  $2B$  in the chiral limit. The middle figure on the right shows the  $F_\pi$  data with no NLO fit far away from the chiral limit. The bottom right figure is the linear fit to the chiral condensate with fitting range  $a \cdot m_q = 0.02 - 0.04$ . The physical fit parameters  $B, F, \Lambda_3$  are discussed in the text.

pseudo-Goldstone spectrum collapsed at fixed gauge coupling. Apparently the NLO operators, the last two terms in Eq. (2.6), have a stronger effect on the spectra relative to leading-order taste breaking operators, the generalization of those from  $N_f = 4$  to  $N_f = 8$  as discussed in Section 2. This somewhat unexpected and unexplained trend is observed for  $N_f > 8$  as well.

We analyzed the  $\chi$ SB pattern within staggered perturbation theory in its generalized form beyond four flavors [60, 61]. The simultaneous chiral fit of  $M_\pi^2/m_q$  and  $F_\pi$  based on Eqs. (2.8-2.11) cannot be done at  $N_f = 8$  within the reach of the largest lattice sizes we deploy since the value of  $F \cdot L_s$  is too small even at  $L_s = 24$ , for gauge couplings where taste breaking drops to an acceptable level. The chiral fit of  $B, F, \Lambda_3$  to  $M_\pi^2/m_q$ , shown at the top right of Fig. 4, is based on Eq. (2.8) only since the  $F_\pi$  data points are outside the convergence range of the chiral expansion. Much larger lattices are required to drop down in  $m_q$  to the region where the simultaneous fit could be made, while maintaining some control over finite volume and taste breaking effects. The finite volume corrections were negligible in the fitted  $a \cdot m_q$  range and Eqs. (2.10,2.11) were not needed.

At  $\beta = 1.4$  the fitted value of  $B$  is  $a \cdot B = 2.6(3)$  in lattice units with  $a \cdot F = 0.0166(9)$  and  $a \cdot \Lambda_3 = 0.48(5)$  also fitted. The fitted  $\rho$ -mass in the chiral limit is  $a \cdot M_\rho = 0.27(2)$  with  $M_\rho/F = 17(1)$ . The fitted value of  $B/F = 158(17)$  is not very reliable but indicates significant enhancement of the chiral condensate from its  $N_f = 4$  value without including renormalization scale effects. The chiral condensate  $\langle \bar{\psi}\psi \rangle$  summed over all flavors is dominated by the linear term in  $m_q$  from UV contributions. The linear fit gives  $\langle \bar{\psi}\psi \rangle = 0.012(1)$  in the chiral limit which differs from the GMOR relation of  $\langle \bar{\psi}\psi \rangle = 8F^2B$  by about a factor of two with  $8F^2B = 0.0058(8)$  fitted. There are several sources of this disagreement which were addressed for the  $N_f = 4$  case earlier. The chiral log in  $\langle \bar{\psi}\psi \rangle$  will bring further down the true fitted value in the chiral limit. Our volumes are not large enough yet to attempt a sensible chiral log fit to the condensate at small  $a \cdot m_q$  values. Finite volume squeezing effects distort the consistency of the results in our limited range of simulation volumes. Similar observations should also be noted when the RMT analysis is applied in the  $\varepsilon$ -regime.

## 5. Goldstone spectrum and $\chi$ SB from simulations at $N_f = 9$ in the p-regime

We had two motivations for the  $N_f = 9$  simulation reported here. We wanted to see whether the rooting procedure (being applied in our project with two fermions in the sextet representation) will present some unexpected changes in the analysis and we were also looking for the continued trends in the  $\chi$ SB pattern. We could not find any noticeable effect from the rooting procedure and the symmetry breaking pattern was consistent with the  $N_f = 8$  simulations.

As shown in Fig. 5 the Goldstone spectrum is still clearly separated from the technicolor scale of the  $\rho$ -meson. The true Goldstone pion and two additional split pseudo-Goldstone states are shown again with different slopes as  $a \cdot m_q$  increases. The trends and the underlying explanation are similar to the  $N_f = 8$  case. The chiral fit to  $M_\pi^2/m_q$  is shown based on Eq. (2.8) only since the  $F_\pi$  data points are outside the convergence range of the chiral expansion. At  $\beta = 2.0$  the fitted value of  $B$  is  $a \cdot B = 2.8(4)$  in lattice units with  $a \cdot F = 0.017(2)$  and  $a \cdot \Lambda_3 = 0.48(9)$  also fitted. The fitted  $\rho$ -mass in the chiral limit is  $a \cdot M_\rho = 0.233(3)$  with  $M_\rho/F = 14(1)$ . The fitted value of  $B/F = 166(32)$  is not very reliable but comparable to the enhancement of the chiral condensate found at  $N_f = 8$  without including renormalization scale effects. Again, at fixed lattice spacing, the small chiral condensate  $\langle \bar{\psi}\psi \rangle$  summed over all flavors is dominated by the linear term in  $m_q$  from UV contributions. The linear fit gives  $\langle \bar{\psi}\psi \rangle = 0.0045(7)$  in the chiral limit which differs from the GMOR relation of  $\langle \bar{\psi}\psi \rangle = 9F^2B$  by about a factor of two with  $9F^2B = 0.007(2)$  fitted. Open issues in the systematics are similar to the  $N_f = 8$  case.

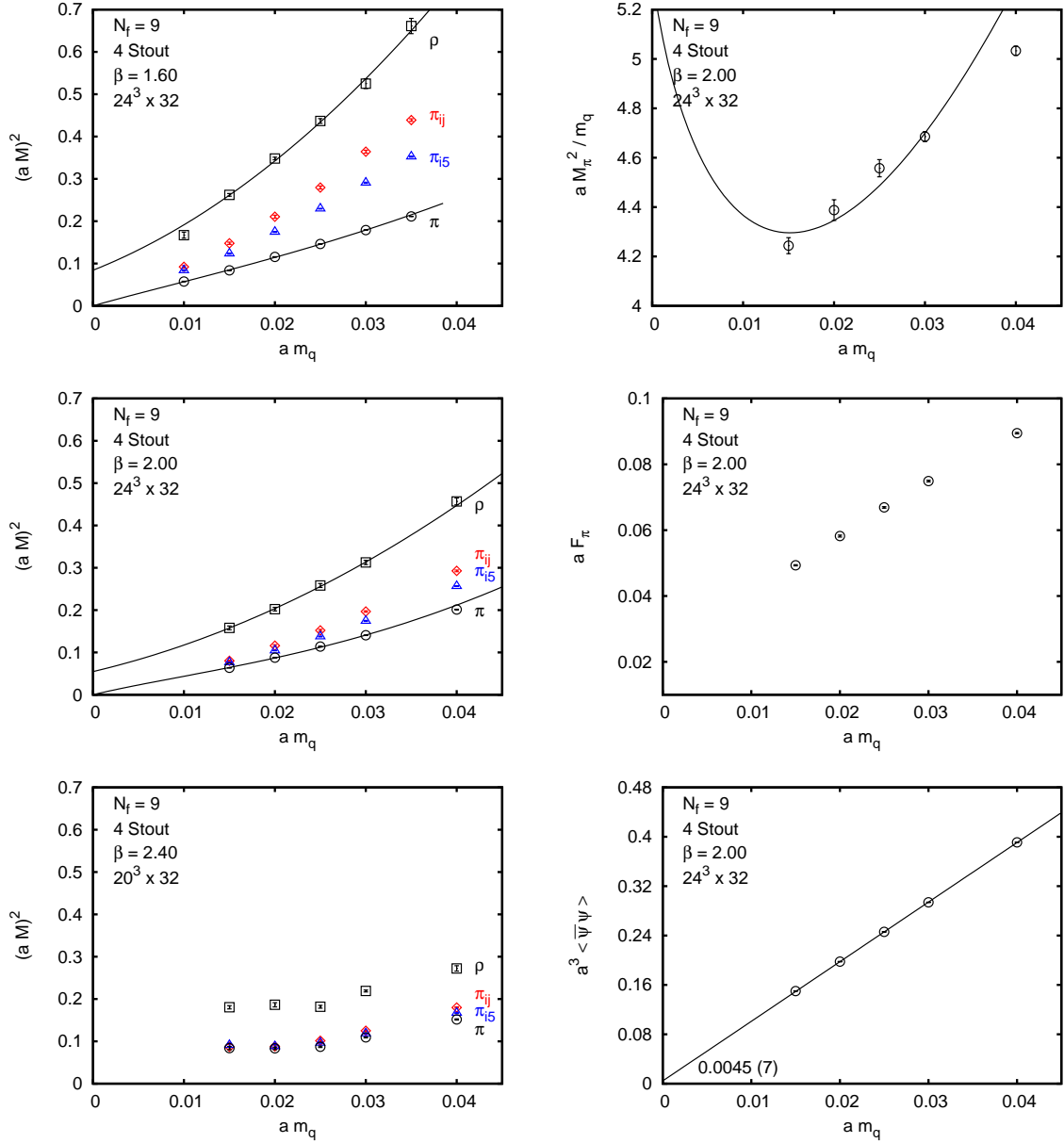


**Figure 5:** The pseudo-Goldstone spectrum and chiral fits are shown for  $N_f = 9$  simulations with lattice size  $24^3 \times 32$ . The left column shows the pseudo-Goldstone spectrum with decreasing taste breaking as the gauge coupling is varied from  $\beta = 1.6$  to  $\beta = 2.4$ . Although the bottom figure on the left at  $\beta = 2.4$  illustrates the continued restoration of taste symmetry, the volume is too small for the Goldstone spectrum. The middle value at  $\beta = 2.0$  was chosen in the top right figure with fitting range  $a \cdot m_q = 0.015 - 0.03$  of the NLO chiral fit to  $M_\pi^2/m_q$  which approaches  $2B$  in the chiral limit. The middle figure on the right shows the  $F_\pi$  data with no NLO fit far away from the chiral limit. The bottom right figure is the linear fit to the chiral condensate with fitting range  $a \cdot m_q = 0.02 - 0.04$ . The physical fit parameters  $B, F, \Lambda_3$  are discussed in the text. Four stout steps were used in all  $N_f = 9$  simulations.

## 6. Goldstone spectrum and $\chi$ SB from simulations at $N_f = 12$ in the p-regime

Finally we move to the controversial  $N_f = 12$  case. We find here a similar chiral symmetry

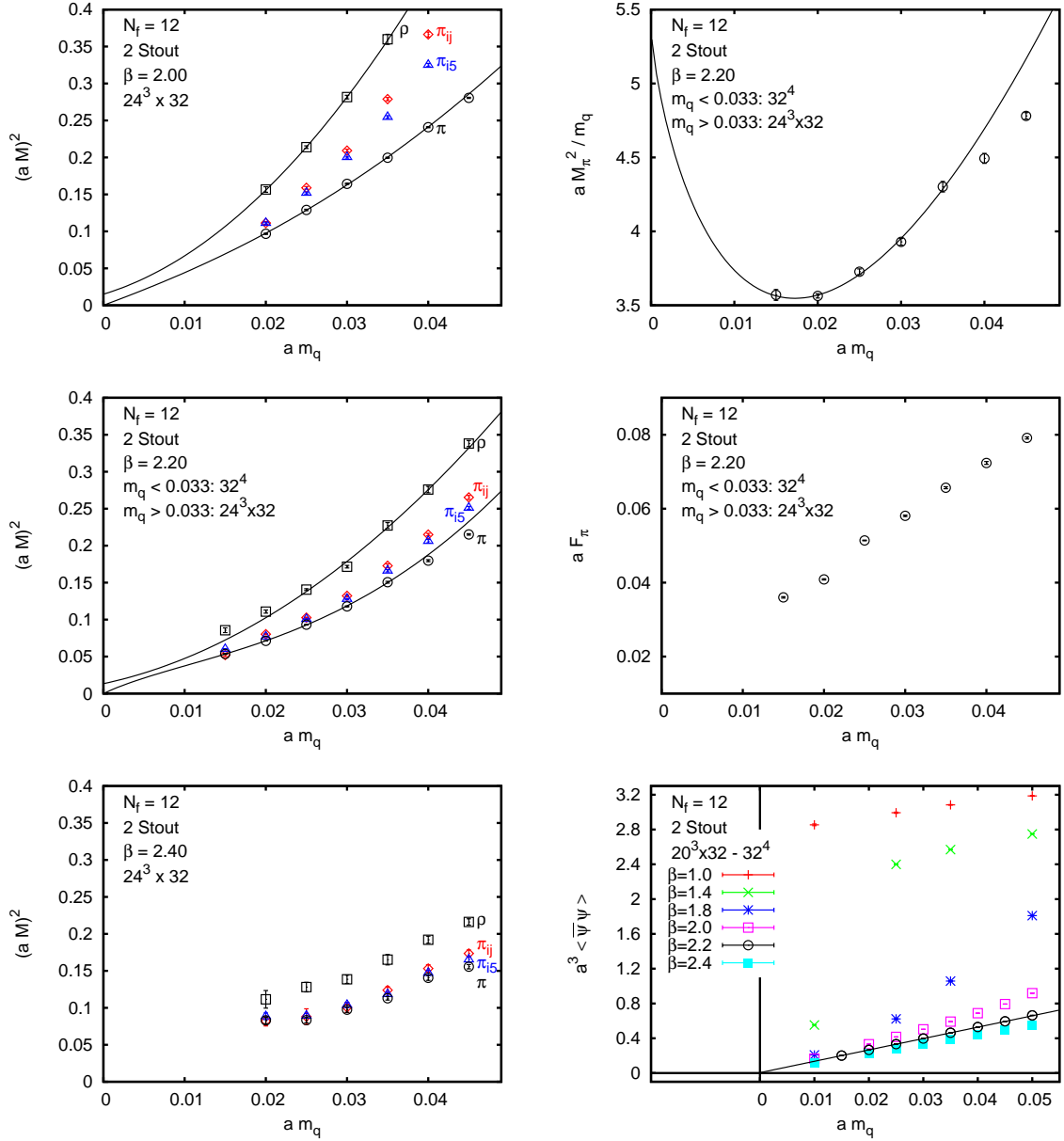


**Figure 6:** The pseudo-Goldstone spectrum and chiral fits are shown for  $N_f = 12$  simulations with lattice size  $24^3 \times 32$  and  $32^4$ . The left column shows the pseudo-Goldstone spectrum with decreasing taste breaking as the gauge coupling is varied from  $\beta = 2.0$  to  $\beta = 2.4$ . Although the bottom figure on the left at  $\beta = 2.4$  illustrates the continued restoration of taste symmetry, the volume is too small for the Goldstone spectrum. The middle value at  $\beta = 2.2$  was chosen in the top right figure with fitting range  $a \cdot m_q = 0.015 - 0.035$  of the NLO chiral fit to  $M_\pi^2/m_q$  which approaches  $2B$  in the chiral limit. The middle figure on the right shows the  $F_\pi$  data with no NLO fit far away from the chiral limit. The bottom right figure, with its additional features discussed in the text, is the linear fit to the chiral condensate with fitting range  $a \cdot m_q = 0.02 - 0.04$ . The physical fit parameters  $B, F, \Lambda_3$  are discussed in the text. Two stout steps were used in all  $N_f = 12$  simulations.

breaking pattern as we found in the  $N_f = 8, 9$  cases with increased concerns about all the caveats presented before. The Goldstone spectrum remains separated from the technicolor scale of the  $\rho$ -meson. The true Goldstone pion and two additional split pseudo-Goldstone states are shown again in Fig. 6 with different slopes as  $a \cdot m_q$  increases. The trends and the underlying explanation are similar to the  $N_f = 8, 9$  cases. The chiral fit to  $M_\pi^2/m_q$  shown at the top right side of Fig. 6 is based on Eq. (2.8) only since the  $F_\pi$  data points are outside the convergence range of the chiral expansion. At  $\beta = 2.2$  the fitted value of  $B$  is  $a \cdot B = 2.7(2)$  in lattice units with  $a \cdot F = 0.0120(1)$  and  $a \cdot \Lambda_3 = 0.50(3)$  also fitted. The fitted  $\rho$ -mass in the chiral limit is  $a \cdot M_\rho = 0.115(15)$  from  $a \cdot m_q = 0.025 - 0.045$  with  $M_\rho/F = 10(1)$ . The fitted value of  $B/F = 223(17)$  is not very reliable but consistent with the enhancement of the chiral condensate found at  $N_f = 8, 9$  without including renormalization scale effects. Again, at fixed lattice spacing, the small chiral condensate  $\langle \bar{\psi}\psi \rangle$  summed over all flavors is dominated by the linear term in  $m_q$  from UV contributions. The linear fit gives  $\langle \bar{\psi}\psi \rangle = 0.0033(13)$  in the chiral limit which came out unexpectedly close the GMOR relation of  $\langle \bar{\psi}\psi \rangle = 12F^2B$  with  $12F^2B = 0.0046(4)$  fitted. Issues and concerns in the systematics are similar to the  $N_f = 8, 9$  cases.

In summary, we have shown strong evidence that according to p-regime tests the  $N_f = 4, 8, 9, 12$  systems all exhibit in the Goldstone and hadron spectra broken chiral symmetry close to the continuum limit. There are some important features of the  $N_f = 12$  analysis which suggest that the model is not only in the  $\chi$ SB phase but also close to slow walking of the renormalized gauge coupling. The bottom right of Fig. 6 shows the crossover in the chiral condensate from strong coupling to the weak coupling regime in the relevant range of  $m_q$ . In combination with the nearly degenerate Goldstone spectrum we find it quite suggestive that around  $\beta = 2.2$  we are close to continuum behavior. In addition, we observe that the fitted value of the  $\rho$ -mass in the chiral limit hardly changes in this region as the gauge coupling is varied (at  $\beta = 2.0$  we fit  $a \cdot M_\rho = 0.123(10)$ ). If confirmed on larger lattices, this could be a first hint of a slowly changing gauge coupling close to the conformal window. Currently we are investigating the important  $N_f = 12$  model on larger lattices to probe the possible influence of unwanted squeezing effects on the spectra. This should also clarify the mass splitting pattern of the  $\rho$  and  $A_1$  states we are seeing in the chiral limit as  $N_f$  is varied.

Our findings at  $N_f = 12$  are in disagreement with [32, 33]. Lessons from the Dirac spectra and RMT to complement p-regime tests are discussed in the next section.

## 7. Epsilon regime, Dirac spectrum and RMT

If the bare parameters of a gauge theory are tuned to the  $\varepsilon$ -regime in the chirally broken phase, the low-lying Dirac spectrum follows the predictions of random matrix theory. The corresponding random matrix model is only sensitive to the pattern of chiral symmetry breaking, the topological charge and the rescaled fermion mass once the eigenvalues are also rescaled by the same factor  $\Sigma_{cond}V$ . This idea has been confirmed in various settings both in quenched and fully dynamical simulations. The same method is applied here to nearly conformal gauge models.

The connection between the eigenvalues  $\lambda$  of the Dirac operator and chiral symmetry breaking is given in the Banks-Casher relation [71],

$$\Sigma_{cond} = -\langle \bar{\Psi}\Psi \rangle = \lim_{\lambda \rightarrow 0} \lim_{m \rightarrow 0} \lim_{V \rightarrow \infty} \frac{\pi \rho(\lambda)}{V},$$

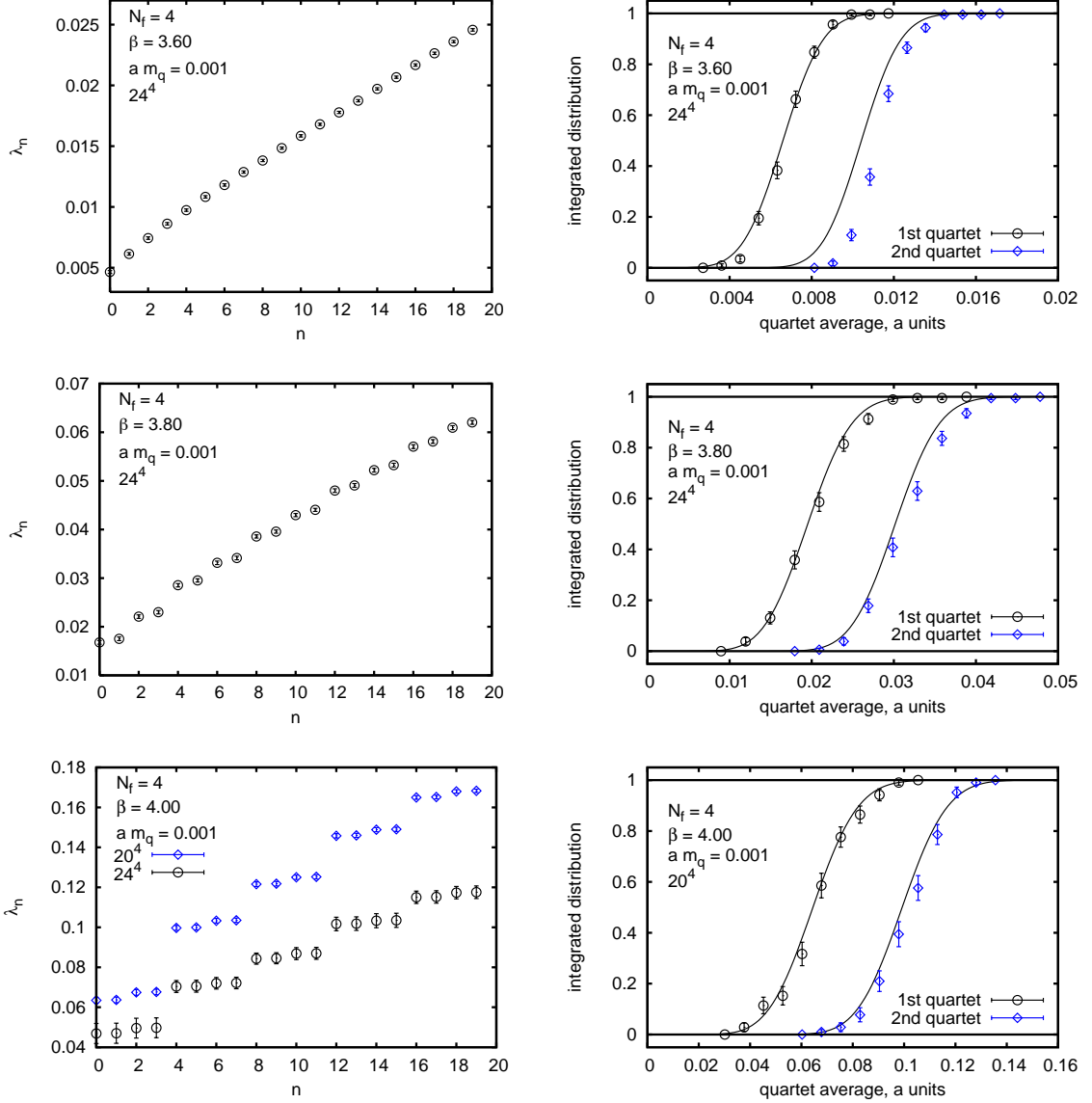


**Figure 7:** From simulations at  $N_f = 4$  the first column shows the approach to quartet degeneracy of the spectrum as  $\beta$  increases. The second column shows the integrated distribution of the two lowest quartets averaged. The solid line compares this procedure to RMT with  $N_f = 4$ .

where  $\Sigma_{cond}$  designates the quark condensate normalized to a single flavor. To generate a non-zero density  $\rho(0)$ , the smallest eigenvalues must become densely packed as the volume increases, with an eigenvalue spacing  $\Delta\lambda \approx 1/\rho(0) = \pi/(\Sigma_{cond}V)$ . This allows a crude estimate of the quark condensate  $\Sigma_{cond}$ . One can do better by exploring the  $\varepsilon$ -regime: If chiral symmetry is spontaneously broken, tune the volume and quark mass such that  $\frac{1}{F_\pi} \ll L \ll \frac{1}{M_\pi}$ , so that the Goldstone pion is much lighter than the physical value, and finite volume effects are dominant as we discussed in Section 2. The chiral Lagrangian of Eq. (2.2) is dominated by the zero-momentum mode from the mass term and all kinetic terms are suppressed. In this limit, the distributions of the lowest

eigenvalues are identical to those of random matrix theory, a theory of large matrices obeying certain symmetries [72, 73, 74]. To connect with RMT, the eigenvalues and quark mass are rescaled as  $z = \lambda \Sigma_{cond} V$  and  $\mu = m_q \Sigma_{cond} V$ , and the eigenvalue distributions also depend on the topological charge  $\nu$  and the number of quark flavors  $N_f$ . RMT is a very useful tool to calculate analytically all of the eigenvalue distributions [75]. The eigenvalue distributions in various topological sectors are measured via lattice simulations, and via comparison with RMT, the value of the condensate  $\Sigma_{cond}$  can be extracted.

After we generate large thermalized ensembles, we calculate the lowest twenty eigenvalues of the Dirac operator using the PRIMME package [76]. In the continuum limit, the staggered eigenvalues form degenerate quartets, with restored taste symmetry. The first column of Fig. 7 shows the change in the eigenvalue structure for  $N_f = 4$  as the coupling constant is varied. At  $\beta = 3.6$  grouping into quartets is not seen, the Goldstone pions are somewhat still split, and staggered perturbation theory is just beginning to kick in. At  $\beta = 3.8$  doublet pairing appears and at  $\beta = 4.0$  the quartets are nearly degenerate. The Dirac spectrum is collapsed as required by the Banks-Casher relation. In the second column we show the integrated distributions of the two lowest eigenvalue quartet averages,

$$\int_0^\lambda p_k(\lambda') d\lambda', \quad k = 1, 2 \quad (7.1)$$

which is only justified close to quartet degeneracy. All low eigenvalues are selected with zero topology. To compare with RMT, we vary  $\mu = m_q \Sigma_{cond} V$  until we satisfy

$$\frac{\langle \lambda_1 \rangle_{sim}}{m} = \frac{\langle z_1 \rangle_{RMT}}{\mu}, \quad (7.2)$$

where  $\langle \lambda_1 \rangle_{sim}$  is the lowest quartet average from simulations and the RMT average  $\langle z \rangle_{RMT}$  depends implicitly on  $\mu$  and  $N_f$ . With this optimal value of  $\mu$ , we can predict the shapes of  $p_k(\lambda)$  and their integrated distributions, and compare to the simulations. The agreement with the two lowest integrated RMT eigenvalue shapes is excellent for the larger  $\beta$  values.

The main qualitative features of the RMT spectrum are very similar in our  $N_f = 8$  simulations as shown in Fig. 8. One marked quantitative difference is a noticeable slowdown in response to change in the coupling constant. As  $\beta$  grows the recovery of the quartet degeneracy is considerably delayed in comparison with the onset of p-regime Goldstone dynamics. Overall, for the  $N_f = 4, 8$  models we find consistency between the p-regime analysis and the RMT tests. Earlier, using Asqtad fermions at a particular  $\beta$  value, we found agreement with RMT even at  $N_f = 12$  which indicated a chirally broken phase [24]. Strong taste breaking with Asqtad fermions leaves the quartet averaging in question and the bulk pronounced crossover of the Asqtad action as  $\beta$  grows is also an issue. Currently we are investigating the RMT picture for  $N_f = 9, 10, 11, 12$  with our much improved action with stout smearing. This action shows no artifact transitions and handles taste breaking much more effectively. Firm conclusions on the  $N_f = 12$  model to support our findings of  $\chi$ SB in the p-regime will require continued investigations.

## 8. Inside the conformal window

We start our investigation and simulations of the conformal window at  $N_f = 16$  which is the most accessible for analytic methods. We are particularly interested in the qualitative behavior of

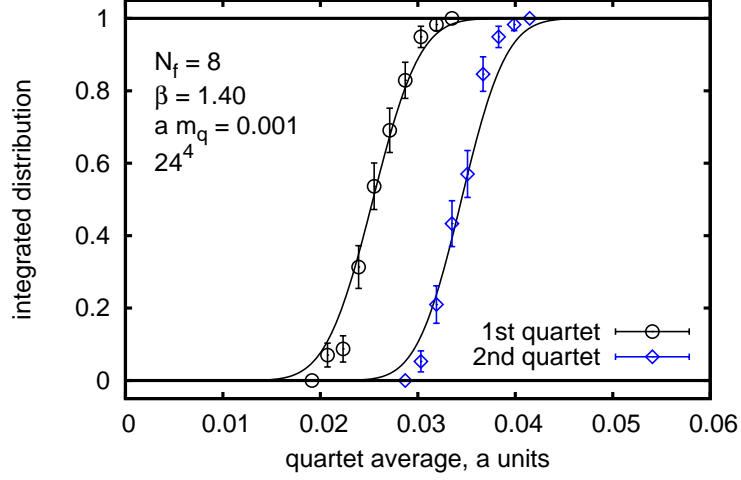


**Figure 8:** The solid lines compare the integrated distribution of the two lowest quartet averages to RMT predictions with  $N_f = 8$ .

the finite volume spectrum of the model and the running coupling with its associated beta function which is expected to have a weak coupling fixed point around  $g^{*2} \approx 0.5$ , as estimated from the scheme-independent, two-loop beta function [77]. A distinguished feature of the  $N_f = 16$  conformal model is how the renormalized coupling  $g^2(L)$  runs with  $L$ , the linear size of the spatial volume in a Hamiltonian or Transfer Matrix description. On very small scales the running coupling  $g^2(L)$  grows with  $L$  as in any other asymptotically free theory. However,  $g^2(L)$  will not grow large, and in the  $L \rightarrow \infty$  limit it will converge to the fixed point  $g^{*2}$  which is rather weak, within the reach of perturbation theory. There is non-trivial, small-volume dynamics which is illustrated first in the pure gauge sector.

At small  $g^2$ , without fermions, the zero-momentum components of the gauge field are known to dominate the dynamics [78, 79, 80]. With  $SU(3)$  gauge group, there are twenty-seven degenerate vacuum states, separated by energy barriers which are generated by the integrated effects of the non-zero momentum components of the gauge field in the Born-Oppenheimer approximation. The lowest-energy excitations of the gauge field Hamiltonian scale as  $\sim g^{2/3}(L)/L$  evolving into glueball states and becoming independent of the volume as the coupling constant grows with  $L$ . Non-trivial dynamics evolves through three stages as  $L$  grows. In the first regime, in very small boxes, tunneling is suppressed between vacua which remain isolated. In the second regime, for larger  $L$ , tunneling sets in and electric flux states will not be exponentially suppressed. Both regimes represent small worlds with zero-momentum spectra separated from higher momentum modes of the theory with energies on the scale of  $2\pi/L$ . At large enough  $L$  the gauge dynamics overcomes the energy barrier, and wave functions spread over the vacuum valley. This third regime is the crossover to confinement where the electric fluxes collapse into thin string states wrapping around the box.

It is likely that a conformal theory with a weak coupling fixed point at  $N_f = 16$  will have only the first two regimes which are common with QCD. Now the calculations have to include fermion loops [81, 82]. The vacuum structure in small enough volumes, for which the wave functional

is sufficiently localized around the vacuum configuration, remains calculable by adding in one-loop order the quantum effects of the fermion field fluctuations. The spatially constant abelian gauge fields parametrizing the vacuum valley are given by  $A_i(\mathbf{x}) = T^a C_i^a / L$  where  $T_a$  are the  $(N-1)$  generators for the Cartan subalgebra of  $SU(N)$ . For  $SU(3)$ ,  $T_1 = \lambda_3/2$  and  $T_2 = \lambda_8/2$ . With  $N_f$  flavors of massless fermion fields the effective potential of the constant mode is given by

$$V_{\text{eff}}^{\mathbf{k}}(\mathbf{C}^b) = \sum_{i>j} V(\mathbf{C}^b [\mu_b^{(i)} - \mu_b^{(j)}]) - N_f \sum_i V(\mathbf{C}^b \mu_b^{(i)} + \pi \mathbf{k}), \quad (8.1)$$

with  $\mathbf{k} = \mathbf{0}$  for periodic, or  $\mathbf{k} = (1, 1, 1)$ , for antiperiodic boundary conditions on the fermion fields. The function  $V(\mathbf{C})$  is the one-loop effective potential for  $N_f = 0$  and the weight vectors  $\mu^{(i)}$  are determined by the eigenvalues of the abelian generators. For  $SU(3)$   $\mu^{(1)} = (1, 1, -2)/\sqrt{12}$  and  $\mu^{(2)} = \frac{1}{2}(1, -1, 0)$ . The correct quantum vacuum is found at the minimum of this effective potential which is dramatically changed by the fermion loop contributions. The Polyakov loop observables

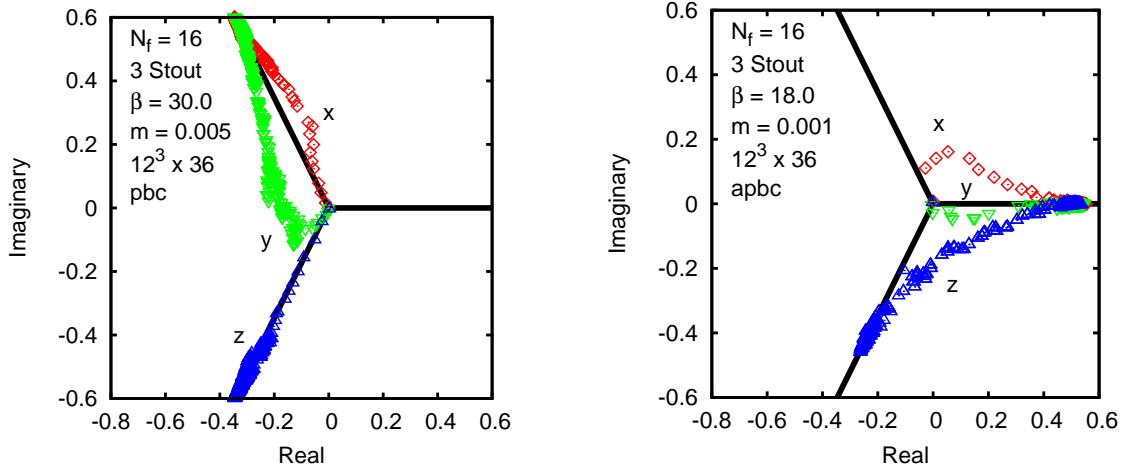


**Figure 9:** The time evolution of complex Polyakov loop distributions are shown from our  $N_f = 16$  simulations with  $12^3 \times 36$  lattice volume. Tree-level Symanzik-improved gauge action is used in the simulations and staggered fermions with three stout steps and very small fermion masses.

remain center elements at the new vacuum configurations with complex values; for  $SU(N)$

$$P_j = \frac{1}{N} \text{tr} \left( \exp(iC_j^b T_b) \right) = \frac{1}{N} \sum_n \exp(i\mu_b^{(n)} C_j^b) = \exp(2\pi i l_j / N). \quad (8.2)$$

This implies  $\mu_b^{(n)} \mathbf{C}^b = 2\pi \mathbf{l} / N \pmod{2\pi}$ , independent of  $n$ , and  $V_{\text{eff}}^{\mathbf{k}} = -N_f N V(2\pi \mathbf{l} / N + \pi \mathbf{k})$ . In the case of antiperiodic boundary conditions,  $\mathbf{k} = (1, 1, 1)$ , this is minimal only when  $\mathbf{l} = \mathbf{0} \pmod{2\pi}$ . The quantum vacuum in this case is the naive one,  $A = 0$  ( $P_j = 1$ ). In the case of periodic boundary conditions,  $\mathbf{k} = \mathbf{0}$ , the vacua have  $\mathbf{l} \neq \mathbf{0}$ , so that  $P_j$  correspond to non-trivial center elements. For  $SU(3)$ , there are now 8 degenerate vacua characterized by eight different Polyakov loops,  $P_j = \exp(\pm 2\pi i / 3)$ . Since they are related by coordinate reflections, in a small volume parity (P) and charge conjugation (C) are spontaneously broken, although CP is still a good symmetry [81].

Our simulations of the  $N_f = 16$  model below the conformal fixed point  $g^{*2}$  confirm the theoretical vacuum structure. Fig. 9 shows the time evolution of Polyakov loop distributions monitored

along the three separate spatial directions. On the left side, with periodic spatial boundary conditions, the time evolution is shown starting from randomized gauge configuration with the Polyakov loop at the origin. The system evolves into one of the eight degenerate vacua selected by the positive imaginary part of the complex Polyakov loop along the x and y direction and negative imaginary part along the z direction. On the right, with antiperiodic spatial boundary conditions, the vacuum is unique and trivial with real Polyakov loop in all three directions. The time evolution is particularly interesting in the z direction with a swing first from the randomized gauge configuration to a complex metastable minimum first, and eventually tunneling back to the trivial vacuum and staying there, as expected. The measured fermion-antifermion spectra and the spectrum of the Dirac operator further confirm this vacuum structure. Our plans include the continued investigation of zero-mode gauge dynamics which should clarify many important aspects of conformal and nearly conformal gauge theories.

## Acknowledgments

We are thankful to Claude Bernard and Steve Sharpe for help with staggered perturbation theory and to Ferenc Niedermayer for discussions on rotator dynamics. We are grateful to Sandor Katz and Kalman Szabo for the Wuppertal RHMC code, and for some calculations, we used the publicly available MILC code. We performed simulations on the Wuppertal GPU cluster, Fermilab clusters under the auspices of USQCD and SciDAC, and the Ranger cluster of the Teragrid organization. This work is supported by the NSF under grant 0704171, by the DOE under grants DOE-FG03-97ER40546, DOE-FG-02-97ER25308, by the DFG under grant FO 502/1 and by SFB-TR/55.

## References

- [1] Z. Fodor, K. Holland, J. Kuti, D. Negradi and C. Schroeder, *Phys. Lett. B* **681**, 353 (2009).
- [2] Z. Fodor, K. Holland, J. Kuti, D. Negradi and C. Schroeder, paper in preparation.
- [3] Z. Fodor, K. Holland, J. Kuti, D. Negradi and C. Schroeder, *PoS LATTICE2009*, 058 (2009).
- [4] S. Weinberg, *Phys. Rev. D* **19**, 1277 (1979).
- [5] L. Susskind, *Phys. Rev. D* **20**, 2619 (1979).
- [6] E. Farhi and L. Susskind, *Phys. Rept.* **74**, 277 (1981).
- [7] F. Sannino, arXiv:0902.3494 [hep-ph].
- [8] T. A. Ryttov and F. Sannino, *Phys. Rev. D* **76**, 105004 (2007).
- [9] D. D. Dietrich and F. Sannino, *Phys. Rev. D* **75**, 085018 (2007).
- [10] D. K. Hong et al., *Phys. Lett. B* **597**, 89 (2004).
- [11] H. Georgi, *Phys. Rev. Lett.* **98**, 221601 (2007).
- [12] M. A. Luty and T. Okui, *JHEP* **0609**, 070 (2006).
- [13] W. E. Caswell, *Phys. Rev. Lett.* **33**, 244 (1974).
- [14] T. Banks and A. Zaks, *Nucl. Phys. B* **196**, 189 (1982).

- [15] T. Appelquist et al., Phys. Rev. Lett. **61**, 1553 (1988).
- [16] A. G. Cohen and H. Georgi, Nucl. Phys. B **314**, 7 (1989).
- [17] T. Appelquist et al., Phys. Rev. Lett. **77**, 1214 (1996).
- [18] B. Holdom, Phys. Rev. D **24**, 1441 (1981).
- [19] K. Yamawaki et al., Phys. Rev. Lett. **56**, 1335 (1986).
- [20] T. W. Appelquist et al., Phys. Rev. Lett. **57**, 957 (1986).
- [21] V. A. Miransky and K. Yamawaki, Phys. Rev. D **55**, 5051 (1997).
- [22] M. Kurachi and R. Shrock, JHEP **0612**, 034 (2006).
- [23] E. Eichten and K. D. Lane, Phys. Lett. B **90**, 125 (1980).
- [24] Z. Fodor et al., PoS **LATTICE2008**, 066 (2008).
- [25] Z. Fodor et al., PoS **LATTICE2008**, 058 (2008).
- [26] Z. Fodor, K. Holland, J. Kuti, D. Nogradi and C. Schroeder, arXiv:0908.2466 [hep-lat].
- [27] Z. Fodor, K. Holland, J. Kuti, D. Nogradi and C. Schroeder, JHEP **0908**, 084 (2009) [arXiv:0905.3586 [hep-lat]].
- [28] T. DeGrand et al., Phys. Rev. D **79**, 034501 (2009).
- [29] T. DeGrand et al., arXiv:0809.2953 [hep-lat].
- [30] B. Svetitsky et al., arXiv:0809.2885 [hep-lat].
- [31] Y. Shamir et al., Phys. Rev. D **78**, 031502 (2008).
- [32] T. Appelquist et al., Phys. Rev. Lett. **100**, 171607 (2008).
- [33] T. Appelquist et al., arXiv:0901.3766 [hep-ph].
- [34] G. T. Fleming, PoS **LATTICE2008**, 021 (2008).
- [35] L. Del Debbio et al., arXiv:0812.0570 [hep-lat].
- [36] L. Del Debbio et al., arXiv:0805.2058 [hep-lat].
- [37] L. Del Debbio et al., JHEP **0806**, 007 (2008).
- [38] A. J. Hietanen et al., arXiv:0904.0864 [hep-lat].
- [39] A. J. Hietanen et al., arXiv:0812.1467 [hep-lat].
- [40] A. Hietanen et al., PoS **LATTICE2008**, 065 (2008).
- [41] A. Deuzeman et al., arXiv:0904.4662 [hep-ph].
- [42] A. Deuzeman et al., arXiv:0810.3117 [hep-lat].
- [43] A. Deuzeman et al., PoS **LATTICE2008**, 060 (2008).
- [44] A. Deuzeman et al., Phys. Lett. B **670**, 41 (2008).
- [45] S. Catterall and F. Sannino, Phys. Rev. D **76**, 034504 (2007).
- [46] S. Catterall et al., JHEP **0811**, 009 (2008).
- [47] X. Y. Jin and R. D. Mawhinney, PoS **LATTICE2008**, 059 (2008).

- [48] A. Hasenfratz, arXiv:0907.0919 [hep-lat].
- [49] T. DeGrand and A. Hasenfratz, arXiv:0906.1976 [hep-lat].
- [50] T. DeGrand, arXiv:0906.4543 [hep-lat].
- [51] L. Del Debbio et al., arXiv:0907.3896 [hep-lat].
- [52] T. DeGrand, arXiv:0910.3072 [hep-lat].
- [53] T. Appelquist *et al.*, arXiv:0910.2224 [hep-ph].
- [54] X. Y. Jin and R. D. Mawhinney, PoS **LAT2009**, 049 (2009).
- [55] A. Hasenfratz, arXiv:0911.0646 [hep-lat].
- [56] D. K. Sinclair and J. B. Kogut, arXiv:0909.2019 [hep-lat].
- [57] C. Morningstar and M. J. Peardon, Phys. Rev. D **69**, 054501 (2004).
- [58] Y. Aoki *et al.*, JHEP **0601**, 089 (2006); Phys. Lett. B **643**, 46 (2006).
- [59] W. J. Lee and S. R. Sharpe, Phys. Rev. D **60**, 114503 (1999).
- [60] C. Aubin and C. Bernard, Phys. Rev. D **68**, 034014 (2003).
- [61] C. Aubin and C. Bernard, Phys. Rev. D **68**, 074011 (2003).
- [62] J. Gasser and H. Leutwyler, Nucl. Phys. B **307**, 763 (1988).
- [63] F. C. Hansen and H. Leutwyler, Nucl. Phys. B **350**, 201 (1991).
- [64] J. Gasser and H. Leutwyler, Annals Phys. **158**, 142 (1984).
- [65] M. Gell-Mann et al., Phys. Rev. **175**, 2195 (1968).
- [66] J. Bijnens and J. Lu, arXiv:0910.5424 [hep-ph].
- [67] H. Leutwyler, Phys. Lett. B **189**, 197 (1987).
- [68] J. Noaki *et al.* [JLQCD and TWQCD Collaborations], Phys. Rev. Lett. **101**, 202004 (2008).
- [69] P. Hasenfratz and F. Niedermayer, Z. Phys. B **92**, 91 (1993), arXiv:hep-lat/9212022.
- [70] P. Hasenfratz, arXiv:0909.3419 [hep-th].
- [71] T. Banks and A. Casher, Nucl. Phys. B **169**, 103 (1980).
- [72] E. V. Shuryak and J. J. M. Verbaarschot, Nucl. Phys. A **560**, 306 (1993).
- [73] P. H. Damgaard, Nucl. Phys. Proc. Suppl. **128**, 47 (2004).
- [74] J. J. M. Verbaarschot and T. Wettig, Ann. Rev. Nucl. Part. Sci. **50**, 343 (2000).
- [75] P. H. Damgaard and S. M. Nishigaki, Phys. Rev. D **63**, 045012 (2001).
- [76] A. Stathopoulos and J. R. McCombs, SIAM J. Sci. Comput., Vol. **29**, No. **5**, 2162 (2007).
- [77] U. M. Heller, Nucl. Phys. Proc. Suppl. **63**, 248 (1998).
- [78] G. 't Hooft, Nucl. Phys. B **153**, 141 (1979).
- [79] M. Luscher, Nucl. Phys. B **219**, 233 (1983).
- [80] P. van Baal and J. Koller, Annals Phys. **174**, 299 (1987).
- [81] P. van Baal, Nucl. Phys. B **307**, 274 (1988).
- [82] J. Kripfganz and C. Michael, Nucl. Phys. B **314**, 25 (1989).